

# Velocity and Speed Correlations in Hamiltonian Flocks

Mathias Casiulis,<sup>1</sup> Marco Tarzia,<sup>1,2</sup> Leticia F. Cugliandolo,<sup>3,2</sup> and Olivier Dauchot<sup>4</sup>

<sup>1</sup>Sorbonne Université, CNRS UMR 7600, Laboratoire de Physique Théorique de la Matière Condensée, LPTMC, 4 place Jussieu, Couloir 12-13, 5me étage, 75252 Paris Cedex 05, France.\*

<sup>2</sup>Institut Universitaire de France, 1 rue Descartes, 75231 Paris Cedex 05, France

<sup>3</sup>Sorbonne Université, CNRS UMR 7589, Laboratoire de Physique Théorique et Hautes Energies, LPTHE, 4 place Jussieu, Couloir 13-14, 5me étage, 75252 Paris Cedex 05, France

<sup>4</sup>Gulliver Lab, UMR CNRS 7083, PSL Research University, ESPCI Paris 10 rue Vauquelin, 75005 Paris, France

(Dated: June 16, 2022)

We study a 2d Hamiltonian fluid made of particles carrying spins coupled to their velocities. At low temperatures and intermediate densities, this conservative system exhibits phase coexistence between a collectively moving droplet and a still gas. The particle displacements within the droplet have remarkably similar correlations to those of birds flocks. The center of mass behaves as an effective self-propelled particle, driven by the droplet's total magnetization. The conservation of a generalized angular momentum leads to rigid rotations, opposite to the fluctuations of the magnetization orientation that, however small, are responsible for the shape and scaling of the correlations.

Flocking, the formation of compact groups of collectively moving individuals, is a hallmark of animal group behavior at very different scales. This phenomenon has long attracted the interest of biologists [1–7], and motivated a large number of theoretical studies, connecting microscopic Vicsek like models [8–10] to continuous theories of the Toner-Tu type [11–15]. On the experimental side, most quantitative data were obtained in artificial systems [16–19]. Indeed, working with large animal groups implies unavoidable difficulties to control experimental conditions and track trajectories. One noticeable exception is the large scale observational and data analysis effort conducted by the Starflag project [20–26]: the individual three-dimensional trajectories of a few thousand birds in compact flocks were obtained and analyzed. In particular, such starling flocks display correlations for the bird speeds and velocities that have been described as being long-ranged and scale-free [20, 26].

The study of collective motion in vibrated polar grains [27, 28] showed that considering the particles' headings and their velocities as distinct, but coupled, degrees of freedom was instrumental to model the experimental observations [17, 29]. It was soon noticed that, in the presence of such coupling, the existence of collective motion *in equilibrium* cannot be immediately ruled out by standard arguments. A Hamiltonian model of particles carrying ferro-magnetically coupled spins, that also interact with their own velocities, was then proposed [30]. Such Hamiltonian exhibits collectively moving polar ground states at  $T = 0$  (for systems of finite sizes) [30], and a rich phase diagram at finite temperature [31], Fig. 1(a), with a coexistence region between a magnetized moving droplet and a disordered still gas, see Figs. 1(b)-(c) and *Movie1.mp4* in the SI.

In this Letter, we show that the velocities and speeds of the particles inside the moving droplet exhibit correlations that are very similar to those observed in bird flocks, Figs. 1(d)-(e), suggesting a possible simple explanation.

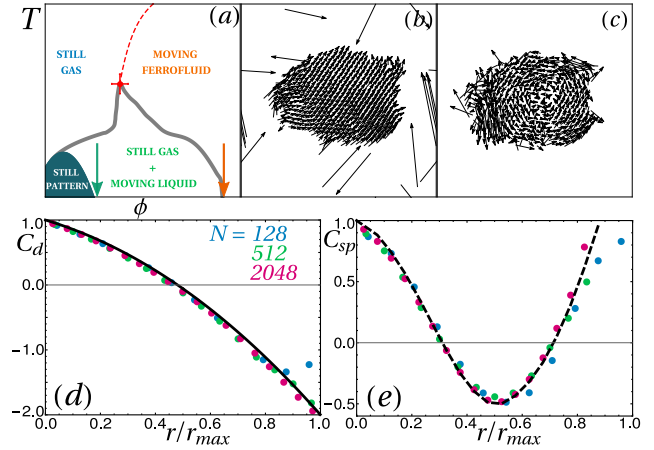


FIG. 1. **Hamiltonian flocks.** (a) Sketch of the phase diagram in the  $(\phi, T)$  plane, for small  $K$  and  $N$ . The orange and teal arrows indicate the densities studied here,  $\phi = 0.55$  and  $\phi = 0.14$ . (b) – (c) Snapshots of the displacements and their fluctuations within a flock ( $N = 512, K = 0.03, T = 10^{-2}$ ). (d) – (e) Spatial correlations  $C_d$  (resp.  $C_{sp}$ ) of the displacement (resp. the speed) fluctuations, against distance normalized by the typical droplet size, for three system sizes ( $T = 10^{-2}$ ). The black lines are our theoretical predictions.

Analyzing the dynamical properties of the model both in the homogeneous polar phase and in the moving droplet phase, we show that the dynamics of the center of mass amount to those of an effective self-propelled particle, driven by the droplet magnetization. The spontaneous fluctuations of this magnetization, together with the conservation of a generalized angular momentum, induce a solid body rotations of the droplet. We show that it is this solid body rotation which, in turn, is responsible for the form and scaling of the displacement correlations. We conclude by discussing the relevance of our findings for real bird flocks.

Our model, first introduced in [30], consists in a system of  $N$  particles, in a 2d periodic square box of linear size  $L_0$ , interacting through an isotropic short-range repulsive

potential  $U(r) = 4(1-r)^4\Theta(1-r)$ , with  $\Theta$  the Heaviside step function. Each particle carries a unit planar vector, or spin,  $\mathbf{s}_i$ , with continuous orientation. The spins are coupled ferro-magnetically through an isotropic short-range coupling  $J(r) = (1-r)^2\Theta(1-r)$ . This ferromagnetic interaction induces an effective attraction at low temperature,  $T$ , resulting in an effective hard radius  $r_0 = 1/4$  at  $T = 0$ . We define the packing fraction  $\phi \equiv \pi N r_0^2 / L_0^2$ . The key ingredient is the introduction of a self-alignment between the spin and the velocity of each particle, through a coupling constant  $K$ . Starting from the Lagrangian formulation (see the SI), we obtain:

$$\mathcal{H} = \sum_{i=1}^N \left( \frac{\mathbf{p}_i^2}{2} + \frac{\omega_i^2}{2} - K \mathbf{p}_i \cdot \mathbf{s}_i \right) + \frac{1}{2} \sum_{k \neq i} [U(r_{ik}) - J(r_{ik}) \mathbf{s}_i \cdot \mathbf{s}_k], \quad (1)$$

where,  $\mathbf{r}_i$  are the positions of the particles,  $r_{ik} = |\mathbf{r}_i - \mathbf{r}_k|$ ,  $\mathbf{s}_i$  their spins parametrized by an angle  $\theta_i$ ,  $\omega_i = \dot{\theta}_i$  the momenta associated to these angles, and  $\mathbf{p}_i = \dot{\mathbf{r}}_i + K \mathbf{s}_i$  the linear momenta associated to the positions.

The dynamics conserve the total energy  $\mathcal{H}$ , the total linear momentum  $\mathbf{P} = \sum_i \mathbf{p}_i = N(\mathbf{v}_G + K\mathbf{m})$ , and the total angular momentum  $\mathbf{L} = \sum_i [\omega_i \hat{\mathbf{e}}_z + \mathbf{r}_i \times \mathbf{v}_i + K \mathbf{r}_i \times \mathbf{s}_i]$ , where  $\mathbf{v}_G = N^{-1} \sum_i \dot{\mathbf{r}}_i$  is the center of mass velocity,  $\mathbf{m} = N^{-1} \sum_i \mathbf{s}_i$  is the intensive magnetization, and  $\hat{\mathbf{e}}_z = \hat{\mathbf{e}}_x \times \hat{\mathbf{e}}_y$  is the out-of-plane unit vector. We perform Molecular Dynamics (MD) simulations in the  $(N, V, E)$  ensemble, using initial conditions such that  $\mathbf{P} = \mathbf{L} = \mathbf{0}$ . For  $K = 0$ , and at sufficiently low packing fraction,  $\phi$ , and temperature,  $T$ , the system undergoes a ferromagnetism-induced phase separation (FIPS) between a ferromagnetic liquid and a paramagnetic gas due to the emergence of an effective attraction generated by the tendency of the spins to align [32]. For  $K > 0$ , a similar phase separation is observed [31] (see also the SI). The conservation of momentum imposes that magnetized phases move collectively with velocity  $\mathbf{v}_G = -K\mathbf{m}$ . As a result, for large values of  $N$  or  $K$ , the high kinetic energy cost of the polar moving states prohibits the existence of magnetized phases, and still patterns, such as vortices or solitons, with locally aligned spins but no global magnetization, emerge [31]. On the contrary, for small enough  $K$  and  $N$ , the system maintains its magnetization, and spontaneously develops a mean velocity for a wide range of  $\phi$  and  $T$ , see Fig. 1(a). In the following we concentrate on this last situation.

In the coexistence regime, the moving phase consists in a moving droplet, surrounded by a still gas. Figure 1(b) displays a typical snapshot of the displacements  $\mathbf{u}_i \equiv \mathbf{r}_i(\tau) - \mathbf{r}_i(0)$ , where  $\tau = 2 \cdot 10^2$ , is chosen such that very fast thermal fluctuations are averaged out. One can observe the strong polarization of the displacements inside the droplet; their polarity, as defined in the context of bird flocks [20, 23] is  $\Phi \equiv N^{-1} \left| \sum_i \mathbf{u}_i / |\mathbf{u}_i| \right| \simeq 0.95$ . More intriguing are the displacement fluctuations,  $\mathbf{u}_i^* \equiv \mathbf{u}_i - \mathbf{u}_G$ ,

where  $\mathbf{u}_G = N^{-1} \sum_k \mathbf{u}_k$ , displayed in Fig. 1(c). They present a clear spatial organization, which we quantify by computing their spatial correlations across the flock:

$$C_d(r) = \frac{1}{c_0} \frac{\sum_{j \neq i} \mathbf{u}_i^* \cdot \mathbf{u}_j^* \delta(r - r_{ij})}{\sum_{j \neq i} \delta(r - r_{ij})}, \quad (2)$$

where  $c_0$  is a normalization factor that ensures  $C_d(0) = 1$  and  $\delta$  is a binning function. Similarly, one defines the speed-speed correlation function,  $C_{sp}(r)$ , by replacing  $\mathbf{u}_i^*$  by  $|\mathbf{u}_i| - N^{-1} \sum |\mathbf{u}_k|$  in the above definition. Figure 1(d)-(e) display  $C_d(r)$  and  $C_{sp}(r)$  against  $r/r_{max}$  for  $N = 128, 512, 2048$  and  $K = 0.03, 0.03, 0.001$ , respectively, with  $r_{max}$  the largest distance between two particles in the droplet. We observe an excellent data collapse, indicating that the only relevant scale is the droplet size.

Such correlations, without any scale other than the system size, were first reported in bird flocks [20]. In the theoretical framework of the Vicsek [8] model and its hydrodynamic description by Toner-Tu [11–13], in which flocking results from the build-up of a true long-range polar order, these correlations have been described as being scale-free, suggesting an underlying critical phenomenon. However, as stated in Ref. [20], while the hydrodynamic theories of flocking are good candidates to explain the correlations of the displacement *vectors*, in particular the ones of their orientations, they do not explain the scale-free nature of the *speed* correlations. Explaining the latter within a critical framework requires either the application of an external dynamical field [21], or the introduction of a free energy with a marginal direction [26].

Although it is clear that the present model is clearly *not* a model of birds, the fact that we recover strikingly similar correlations suggests a possibly simpler and unified explanation of the speed and velocity correlations. We start with a quantitative description of the structure and dynamics of the homogeneous moving phase, and then we focus on the inhomogeneous one. To address the first case, we choose  $\phi = 0.55$  (orange arrow in Fig. 1(e)) with  $N = 128$  and  $K = 0.23$ . When decreasing the temperature, the system first magnetizes (Fig. 2(a)) at a crossover taking place at  $T \approx 10^{-1}$ . At even lower  $T$  ( $T \leq 2 \cdot 10^{-2}$ ) a structural organization takes place, as testified by the growth of the hexatic order parameter  $\Psi_6$  [33], symptomatic of a 2d system approaching a solid phase (Fig. 2(b)). The dynamics are then characterized for a few values of  $T$ , indicated by arrows in Fig. 2(a)-(b). The Mean Square Displacements (MSD) relative to the center of mass,  $\Delta r^{*2}(t)$ , shown in Fig. 2(c) are the ones of a usual fluid: they cross over from a short-time ballistic regime to a long-time diffusive regime, and feature finite plateaus at low  $T$ s, revealing the freezing of the dynamics as the system becomes solid [34, 35]. The Mean Square Angular Displacements (MSAD) associated to the spin fluctua-

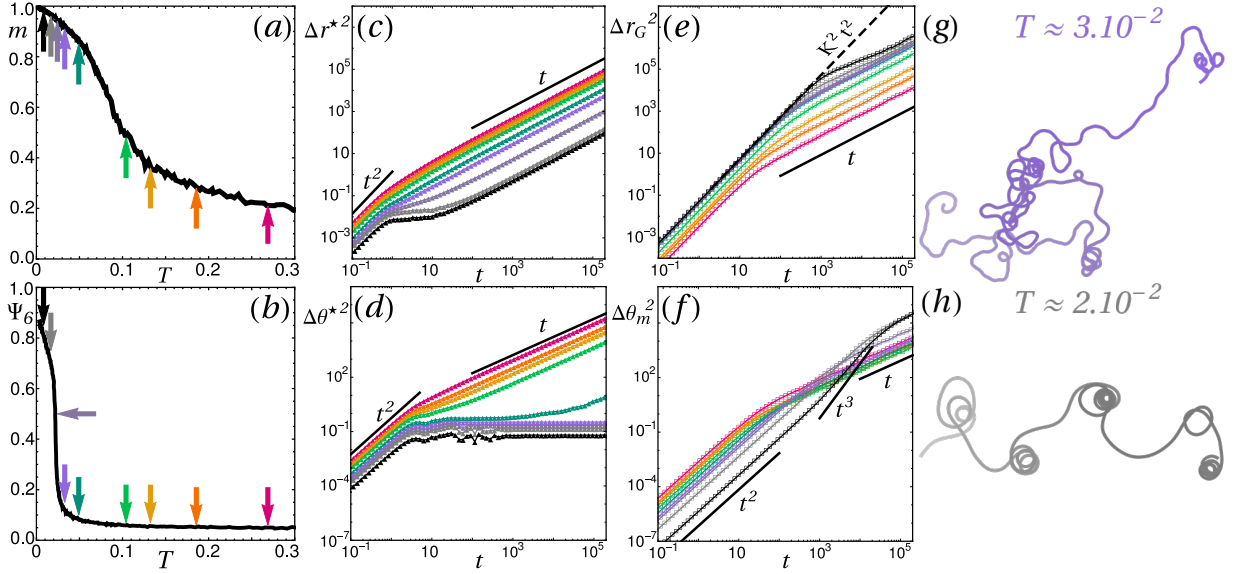


FIG. 2. **Dynamics and Structure of the Homogeneous phases.** (a) Mean magnetization modulus and (b) hexatic order parameter versus  $T$ . The arrows indicate the  $T$  values at which the MSD curves in (c) – (f) are recorded. (c) MSD and (d) MSAD of the relative displacements versus time, in log-log scale. (e) MSD of the center of mass (the dashed black line indicates  $v_G = K$ ), and (f) MSAD of the magnetization vector versus time, in log-log scale. (g) – (h) Trajectories of the center of mass, with time going from light to dark, for two temperatures corresponding to the (g) mauve and (h) light gray curves in (c) – (f).  $N = 128, K = 0.23$ .

tions around the mean magnetization,  $\Delta\theta^{*2}(t)$  shown in Fig. 2(d), behave like the MSD, except that the plateaus develop at the magnetization crossover: spin-wave excitations are exponentially suppressed as the temperature decreases [36], similarly to what we found for  $K = 0$  [32]. The MSD of the center of mass,  $\Delta r_G^2(t)$ , characterizes the collective motion of the droplet (Fig. 2(e)). At short times the motion is ballistic, with a collective speed  $v_G = Km$  due to momentum conservation. At long times it becomes diffusive, with a diffusion coefficient that grows as  $T$  decreases. At very low  $T$ , one notices the presence of a short sub-diffusive regime, which separates the ballistic from the diffusive regime. Finally, the MSAD  $\Delta\theta_m^2(t)$  associated to the orientation of the magnetization,  $\theta_m = \text{atan}(m_y/m_x)$  (Fig. 2(f)) is ballistic at short times, showing that the magnetization follows inertial dynamics, and diffusive at long times, with a diffusion constant which decreases with decreasing  $T$  as long as the system is paramagnetic, and increases when further decreasing  $T$  into the ferromagnetic phase. At very low  $T$ , one also notices the presence of a short super-ballistic regime. This unusual intermediate regime develops at the liquid-solid crossover, concomitantly with the sub-diffusive regime of  $\Delta r_G^2$ . The trajectories of the center of mass give a first hint of its origin. In the isotropic liquid, Fig. 2(g), the trajectories look like persistent random walks whereas, as the system becomes rigid, Fig. 2(h), loops in which the rotation of  $\mathbf{m}$  accelerates appear, leading to a less efficient exploration of space.

The role played by the onset of rigidity can be rationalized, writing down an effective model for the dynamics of the center of mass. We recall that the angular

momentum is conserved. Decomposing the positions, spins and velocities as  $\mathbf{r}_i = \mathbf{r}_G + \mathbf{r}_i^*$ ,  $\mathbf{s}_i = \mathbf{m} + \delta\mathbf{s}_i$  and  $\mathbf{v}_i = -K\mathbf{m} + \mathbf{r}_i^* \Omega \hat{\mathbf{e}}_{\phi,i} + \delta\mathbf{v}_i$ , with  $\Omega$  the mean rotational velocity and  $\hat{\mathbf{e}}_{\phi,i} = \hat{\mathbf{e}}_z \times \mathbf{r}_i/r_i$ , and using that  $\mathbf{P} = \mathbf{0}$ , the angular momentum reads

$$\mathbf{L} = N\dot{\theta}_m \hat{\mathbf{e}}_z + I\Omega \hat{\mathbf{e}}_z + \delta\mathbf{L}, \quad (3)$$

where  $I = \sum r_i^2$  is the moment of inertia, and  $\delta\mathbf{L} = \sum \mathbf{r}_i^* \times (\delta\mathbf{v}_i + K\delta\mathbf{s}_i)$ . Assuming that  $\Omega \approx f\dot{\theta}_m$ , with  $f$  a constant, approximating  $\delta\dot{\mathbf{L}}$  by a noise term, and introducing a characteristic time  $\tau_m \sim (N + fI)/(fI)$ , that we treat as a constant, the conservation of momentum  $\dot{\mathbf{L}} = \mathbf{0}$  reads

$$\tau_m \ddot{\theta}_m + \dot{\theta}_m = \sqrt{D_r} \eta_m, \quad (4)$$

where  $D_r$  is a rotational diffusion constant, and  $\eta_m$  a centered Gaussian white noise. All in all, neglecting for simplicity the fluctuations of the magnetization amplitude, the dynamics of the center of mass obey the equation  $\mathbf{v}_G = -Km(T)\hat{\mathbf{e}}_m$  where  $\hat{\mathbf{e}}_m$ , the orientation of  $\mathbf{m}$ , follows the dynamics prescribed by Eq. (4). This equation states that  $\theta_m$  is subject to inertia and rotational diffusion and defines an Angular Velocity Ornstein-Uhlenbeck Particles (AVOUP), a model similar to the ones used to describe experimental living systems, ranging from microtubules to flatworms [37–40]. Here, the inertial time  $\tau_m$  not only grows as the moment of inertia increases, but also as the deformation dynamics (encoded by  $I$ ) are suppressed: in other words, it increases as the system becomes rigid. The associated accelerated dynamics of  $\theta_m$  is responsible for the super-ballistic regime observed for  $\Delta\theta_m(t)$  and, in turn, the sub-diffusive regime for  $\Delta r_G(t)$ .

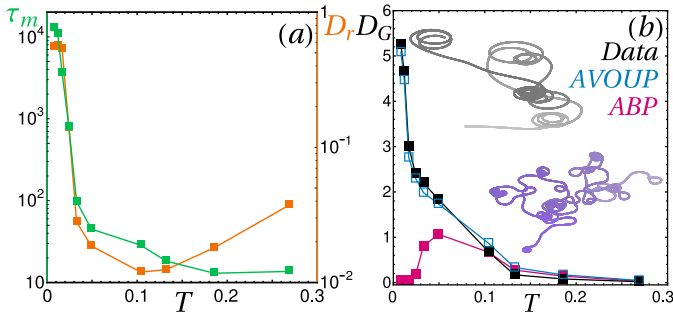


FIG. 3. **AVOUPs Dynamics.** (a)  $\tau_m$  (green) and  $D_r$  (orange) versus  $T$  in lin-log scale. (b)  $D_G$  against  $T$  (black), together with the ABP (red) and AVOUP (blue) estimations. Inset: Trajectories, with time going from light to dark, obtained by integrating the AVOUP equations of motion over  $t = 10000$ , with an integration step  $\delta t = 1$ , and fixed values  $Km = 0.1, D_r = 1$ .  $\tau_m = 5000$  (gray), and  $\tau_m = 500$  (mauve).

In fact, the large inertia limit,  $\tau_m \rightarrow \infty$ , yields a random-acceleration process, that behaves like  $\Delta\theta_m^2 \sim t^3$  at long times [41]. This regime was recently related to looping trajectories in a study of self-propulsion with memory [42].

We further validate our effective description by comparing the diffusion constant of the center of mass,  $D_G$ , obtained from the MD simulations, with the theoretical prescription for AVOUP [43]:

$$D_G^{\text{AVOUP}} = D_G^{\text{ABP}} \Gamma(\tau_m D_r) \sum_{n=0}^{\infty} \frac{(\tau_m D_r)^{n+1}}{\Gamma(n+1 + \tau_m D_r)}, \quad (5)$$

where we introduced the  $\Gamma$ -function and  $D_G^{\text{ABP}} = K^2 m^2 / (2D_r)$  is the diffusion constant in the over-damped limit of Active Brownian Particles (ABP) [44, 45]. We extract  $D_r$  from the long-time diffusive behavior of  $\theta_m$ , and  $\tau_m$  from a short-time exponential fit of the two-time autocorrelation  $C(t) = \langle \dot{\theta}_m(0)\dot{\theta}_m(t) \rangle$ . These inputs are plotted against  $T$  in Fig. 3(a). Note that  $\tau_m$  rises concomitantly with  $\Psi_6$ , confirming that the inertia of  $\theta_m$  is tightly related to the rigidity of the system. Figure 3(b) shows how good the AVOUP estimation of  $D_G$  is, while the zero-memory limit is essentially only valid at high  $T$ , where the magnetization is low. The trajectories obtained by integrating the AVOUPs dynamics for two  $\tau_m$  also are good reproductions of the trajectories shown in Fig. 2.

Coming back to the phase-separated states, say at  $\phi = 0.14, N = 128$ , and  $K = 0.03$ , we observe that the AVOUP description and the general features of the center of mass trajectories are almost unchanged, see Fig. 4. The only major difference occurs at very low  $T$ , where the droplet is highly magnetized, structurally ordered, dynamically frozen, and immersed in a very low density gas. Under these circumstances, the relative displacements exhibit an intermediate second ballistic regime, that can also be explained by the conservation of  $L$ . As an individual flock is free to rotate around its center of mass,

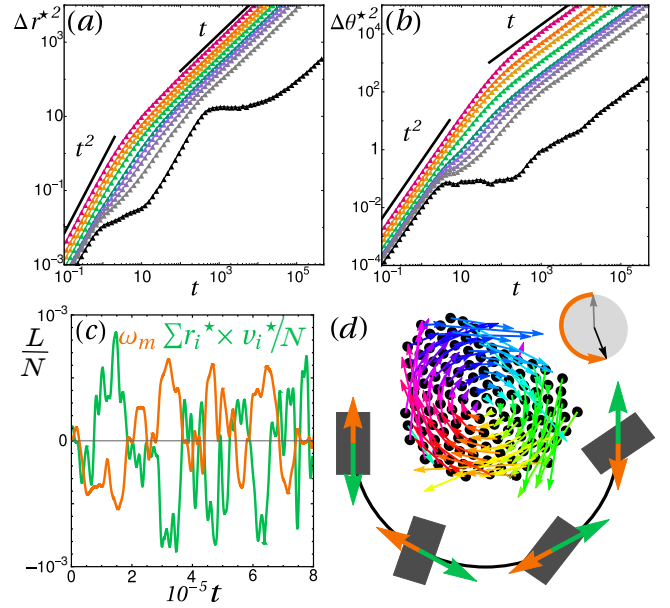


FIG. 4. **Spontaneous Rigid Rotations.** Relative (a) MSD and (b) MSAD for  $N = 128, K = 0.03, \phi \approx 0.14$  and  $T$  increasing from black to red. (c) Typical  $\omega_m = \dot{\theta}_m$  (orange) and  $N^{-1} \sum \mathbf{r}_i^* \times \mathbf{v}_i^*$  (green), time-averaged over  $\tau_w = 10^2$ , versus time. (d) Relative displacements color-coded according to their orientation and rescaled by their mean ( $T \approx 10^{-2}, \tau \approx 10^4$ ), together with a sketch of the spontaneous rotation dynamics, (with  $\mathbf{m}$  in orange and  $\mathbf{v}_G$  in green). Upper inset: the rotation of  $\mathbf{m}$  from the gray to the black arrow, following the orange curved arrow.

a rotation of the magnetization must be compensated by either a solid rotation in the opposite direction or thermal fluctuations [see Eq. (3)]. At very low  $T$ , the thermal fluctuations are no longer enough to absorb changes in  $\dot{\theta}_m$ . As a result, for  $L = 0$ , the droplets develop solid rotations such that  $N\dot{\theta}_m = -I\Omega$ , as confirmed when plotting time-averaged versions of  $\dot{\theta}_m$  and  $N^{-1} \sum \mathbf{r}_i^* \times \mathbf{v}_i^*$  Fig. 4(c). The associated displacement fields, Fig. 4(d), explain our initial observations, Fig. 1(d)-(e): a rigid rotation yields a correlation of the relative displacements at the scale of the size of the system (see also *Movie2.mp4* in the SI). The excellent matching between the numerically observed correlations and the calculation of  $C_d$  and  $C_{sp}$  for a homogeneous rigid disk rotating at a constant rate (see the SI), shown with black lines in Fig. 1(d)-(e), confirms the above interpretation.

All in all, we showed that correlations remarkably similar to those observed in flocks of birds, with no other scale than the droplet size itself, such as those observed in flocks of birds are also observed in Hamiltonian flocks. However, in the present case, the scaling and specific functional form of these correlations are caused by the solid body rotation of the flock. This result contrasts with the interpretation inspired by magnetism and critical phenomena whereby the “scale-free” character of  $C_d$  has been attributed to the Goldstone mode along the longitudinal direction of an effective potential [20, 25], while the one of  $C_{sp}$  to the marginality of its transverse direc-

tion [26]. Our result suggests a different view: these correlations could be attributed to *any small* amount of rigid rotation of the flock. Several experimental observations on bird flocks back this interpretation. First, on short time scales, the flocks do not rearrange [21, 25]: they are solid. Second, data provided in the SI of Ref. [20], demonstrate that there is some rotation in the displacement field, as well as a quadripolar-like field (see the data analysis in the SI). Therefore, flocks of birds could perhaps be seen as elastic solids on short enough time scales. Let us finally stress that the solid body rotation can have very different origins. In the case of Hamiltonian flocks, it is rooted in the angular momentum conservation. Nevertheless, the latter does not seem to be necessary: clusters with solid body rotations have also been reported in self-propelled Janus colloids [46, 47] and active dumbbell models [48], non-conservative systems with no strict angular momentum conservation. Having said this, whether the invariance under rotations of active systems leads to pseudo-conserved generalized angular momenta remains to be elucidated.

We thank A. Jelić for useful discussions.

---

\* [casiulis@lptmc.jussieu.fr](mailto:casiulis@lptmc.jussieu.fr)

- [1] C. M. Breder Jr, *Ecology* **35**, 361 (1954).
- [2] I. Aoki, *Nippon Suisan Gakkaishi* **48**, 1081 (1982).
- [3] J. P. Badgerow, *Auk* **105**, 749 (1988).
- [4] A. Huth and C. Wissel, *J. Theor. Biol.* **156**, 365 (1992).
- [5] J. Krause and G. D. Ruxton, *Living in Groups* (Oxford University Press, Oxford, 2002).
- [6] K. Tunstrøm, Y. Katz, C. C. Ioannou, C. Huepe, M. J. Lutz, and I. D. Couzin, *PLoS Comput. Biol.* **9**, e1002915 (2013).
- [7] S. B. Rosenthal, C. R. Twomey, A. T. Hartnett, H. S. Wu, and I. D. Couzin, *Proc. Natl. Acad. Sci. U. S. A.* **112**, 4690 (2015).
- [8] T. Vicsek, A. Czirók, E. Ben-Jacob, I. Cohen, and O. Shochet, *Phys. Rev. Lett.* **75**, 1226 (1995).
- [9] G. Grégoire and H. Chaté, *Phys. Rev. Lett.* **92**, 025702 (2004).
- [10] T. Vicsek and A. Zafeiris, *Phys. Rep.* **517**, 71 (2012).
- [11] J. Toner and Y. Tu, *Phys. Rev. Lett.* **75**, 4326 (1995).
- [12] Y. Tu, J. Toner, and M. Ulm, *Phys. Rev. Lett.* **80**, 4819 (1998).
- [13] J. Toner, Y. Tu, and S. Ramaswamy, *Ann. Phys. (N. Y.)* **318**, 170 (2005).
- [14] A. Peshkov, E. Bertin, F. Ginelli, and H. Chaté, *Eur. Phys. J. Spec. Top.* **223**, 1315 (2014).
- [15] M. C. Marchetti, J. F. Joanny, S. Ramaswamy, T. B. Liverpool, J. Prost, M. Rao, and R. A. Simha, *Rev. Mod. Phys.* **85**, 1143(47) (2013).
- [16] V. Schaller, C. Weber, C. Semmrich, E. Frey, and A. R. Bausch, *Nature* **467**, 73 (2010).
- [17] J. Deseigne, O. Dauchot, and H. Chaté, *Phys. Rev. Lett.* **105**, 098001 (2010).
- [18] A. Bricard, J.-B. Caussin, N. Desreumaux, O. Dauchot, and D. Bartolo, *Nature* **503**, 95 (2013).
- [19] D. Geyer, A. Morin, and D. Bartolo, *Nat. Mater.* **17**, 789 (2018).
- [20] A. Cavagna, A. Cimarelli, I. Giardina, G. Parisi, R. Santagati, F. Stefanini, and M. Viale, *Proc. Natl. Acad. Sci.* **107**, 11865 (2010).
- [21] A. Cavagna, S. M. D. Queiros, I. Giardina, F. Stefanini, and M. Viale, *Proc. R. Soc. B Biol. Sci.* **280**, 20122484 (2013).
- [22] A. Attanasi, A. Cavagna, L. Del Castello, I. Giardina, T. S. Grigera, A. Jelic, S. Melillo, L. Parisi, O. Pohl, E. Shen, and M. Viale, *Nat. Phys.* **10**, 691 (2014).
- [23] C. K. Hemelrijk and H. Hildenbrandt, *J. Stat. Phys.* **158**, 563 (2014).
- [24] A. Attanasi, A. Cavagna, L. Del Castello, I. Giardina, A. Jelic, S. Melillo, L. Parisi, O. Pohl, E. Shen, and M. Viale, *J. R. Soc. Interface* **12**, 20150319 (2015).
- [25] A. Cavagna, I. Giardina, and T. S. Grigera, *Phys. Rep.* **728**, 1 (2018).
- [26] A. Cavagna, A. Culla, L. Di Carlo, I. Giardina, and T. S. Grigera, *Comptes Rendus Phys.* **20**, 319 (2019).
- [27] J. Deseigne, S. Léonard, O. Dauchot, and H. Chaté, *Soft Matter* **8**, 5629 (2012).
- [28] C. A. Weber, T. Hanke, J. Deseigne, S. Léonard, O. Dauchot, E. Frey, and H. Chaté, *Phys. Rev. Lett.* **110**, 208001 (2013).
- [29] C. Scholz, S. Jahanshahi, A. Ldov, and H. Löwen, *Nat. Commun.* **9**, 5156 (2018).
- [30] S. L. Bore, M. Schindler, K.-D. N. T. Lam, E. Bertin, and O. Dauchot, *J. Stat. Mech. Theory Exp.* **2016**, 033305 (2016).
- [31] M. Casiulis, M. Tarzia, L. F. Cugliandolo, and O. Dauchot, *Arxiv Prepr.*, 1905.0857 (2019).
- [32] M. Casiulis, M. Tarzia, L. F. Cugliandolo, and O. Dauchot, *J. Chem. Phys.* **150**, 154501 (2019).
- [33] B. I. Halperin and D. R. Nelson, *Phys. Rev. Lett.* **41**, 121 (1978).
- [34] W. van Meegen, T. C. Mortensen, S. R. Williams, and J. Müller, *Phys. Rev. E - Stat. Physics, Plasmas, Fluids, Relat. Interdiscip. Top.* **58**, 6073 (1998).
- [35] M. J. Sánchez-Miranda, B. Bonilla-Capilla, E. Sarmiento-Gómez, E. Lázaro-Lázaro, A. Ramírez-Saito, M. Medina-Noyola, and J. L. Arauz-Lara, *Soft Matter* **11**, 655 (2015).
- [36] J. Tobochnik and G. V. Chester, *Phys. Rev. B* **20**, 3761 (1979).
- [37] Y. Sumino, K. H. Nagai, Y. Shitaka, D. Tanaka, K. Yoshikawa, H. Chaté, and K. Oiwa, *Nature* **483**, 448 (2012).
- [38] K. H. Nagai, Y. Sumino, R. Montagne, I. S. Aranson, and H. Chaté, *Phys. Rev. Lett.* **114**, 168001 (2015).
- [39] C. Chen, S. Liu, X. Q. Shi, H. Chaté, and Y. Wu, *Nature* **542**, 210 (2017).
- [40] T. Sugi, H. Ito, M. Nishimura, and K. H. Nagai, *Nat. Commun.* **10**, 683 (2019).
- [41] T. W. Burkhardt, *J. Stat. Mech. Theory Exp.*, P07004 (2007).
- [42] W. T. Kranz and R. Golestanian, *J. Chem. Phys.* **150**, 214111 (2019).
- [43] P. K. Ghosh, Y. Li, G. Marchegiani, and F. Marchesoni, *J. Chem. Phys.* **143**, 211101 (2015).
- [44] Y. Fily and M. C. Marchetti, *Phys. Rev. Lett.* **108**, 1 (2012).
- [45] R. G. Winkler, A. Wysocki, and G. Gompper, *Soft Matter* **11**, 6680 (2015).
- [46] F. Ginot, I. Theurkauff, F. Detcheverry, C. Ybert, and C. Cottin-Bizonne, *Nat. Commun.* **9**, 696 (2018).
- [47] M. N. van der Linden, L. C. Alexander, D. G. A. L. Aarts, and O. Dauchot, *Phys. Rev. Lett.* **123**, 98001 (2019).
- [48] I. Petrelli, P. Digregorio, L. F. Cugliandolo, G. Gonnella, and A. Suma, *Eur. Phys. J. E* **41**, 128 (2018).

**Supplementary Information for  
“Velocity and Speed Correlations in Hamiltonian Flocks”**

Mathias Casiulis

*Sorbonne Université, CNRS UMR 7600, Laboratoire de Physique Théorique de la Matière Condensée,  
LPTMC, 4 place Jussieu, Couloir 12-13, 5me étage, 75252 Paris Cedex 05, France\**

Marco Tarzia

*Sorbonne Université, CNRS UMR 7600, Laboratoire de Physique Théorique de la Matière Condensée,  
LPTMC, 4 place Jussieu, Couloir 12-13, 5me étage, 75252 Paris Cedex 05, France\* and  
Institut Universitaire de France, 1 rue Descartes, 75231 Paris Cedex 05, France*

Leticia F. Cugliandolo

*Sorbonne Université, CNRS UMR 7589, Laboratoire de Physique Théorique et Hautes Energies,  
LPTHE, 4 place Jussieu, Couloir 13-14, 5me étage, 75252 Paris Cedex 05, France and  
Institut Universitaire de France, 1 rue Descartes, 75231 Paris Cedex 05, France*

Olivier Dauchot

*UMR Gulliver 7083 CNRS, ESPCI Paris, PSL Research University, 10 rue Vauquelin, 75005 Paris, France  
(Dated: June 16, 2022)*

## I. MOVIE CAPTIONS

*Movie1.mp4* – Consecutive snapshots of a system of  $N = 512$  particles, with  $K = 0.03$ , at a packing fraction  $\phi \approx 0.15$ , as obtained from Molecular Dynamics at temperature  $T \approx 1 \cdot 10^{-2}$ . Consecutive snapshots are separated by a time  $\Delta t = 50$  in the rescaled units defined in Sec. II. Particles are color-coded according to the direction of their spin, and a large black arrow represents the total magnetization of the system. The periodic boundary conditions were unwound, so that net displacements are easier to see.

*Movie2.mp4* – Same as in the previous movie, except this time the snapshots are centered on the center of mass of the system, so that only rotational and deformational motions are represented. The total magnetization is this time represented on a tagged particle for readability.

## II. FROM THE LAGRANGIAN TO THE HAMILTONIAN DESCRIPTION

In the main text we discuss the properties of a Hamiltonian system derived from its original definition in the Lagrangian formalism:<sup>1,2</sup>

$$\mathcal{L} = \sum_{i=1}^N \frac{m}{2} \dot{\mathbf{r}}_i^2 + \sum_{i=1}^N \frac{I}{2} \dot{\mathbf{s}}_i^2 + \sum_{i=1}^N K \dot{\mathbf{r}}_i \cdot \mathbf{s}_i - \frac{U_0}{2} \sum_{k \neq i} U(r_{ik}) + \frac{J_0}{2} \sum_{k \neq i} J(r_{ik}) \cos \theta_{ik}. \quad (1)$$

The model describes the dynamics of  $N$  interacting particles confined to move in a  $2d$  periodic square box of linear size  $L$ . The particles carry continuous planar spins with unit modulus. We call  $\mathbf{r}_i$  the position of the  $i$ th particle, and  $\dot{\mathbf{r}}_i$  its velocity. We note  $r_{ik} = |\mathbf{r}_i - \mathbf{r}_k|$  the distance between the centers of the particles  $i$  and  $k$ .  $\theta_i$  is the angle that the spin forms with a reference axis and fully parametrizes the continuous  $2d$  spin  $\mathbf{s}_i$  of unit modulus. The time derivative of the spin vector is indicated by  $\dot{\mathbf{s}}_i$ . Finally,  $\theta_{ik}$  is the angle between the spin of particle  $i$  and the one of particle  $k$ . The model has several parameters and two potentials.  $m$  is the mass of each particle and  $I$  its moment of inertia.  $U$  is a short-ranged, isotropic and purely repulsive two-body interaction potential and  $J$  is a short-ranged and isotropic ferromagnetic coupling between the spins and we have extracted their strengths as the parameters  $U_0$  and  $J_0$ . Following the choices of Refs. [1–3] we use the forms

$$\begin{aligned} J(r) &= (\sigma - r)^2 \Theta(\sigma - r), \\ U(r) &= (\sigma - r)^4 \Theta(\sigma - r), \end{aligned} \quad (2)$$

where  $\Theta$  is a Heaviside step function. These potentials ensure well-behaved discretized Hamiltonian dynamics since they smoothly decrease to zero.  $\sigma$  is a range that was fixed to 1, resulting in an effective hard radius  $r_0 = \sigma/4 = 1/4$  at zero temperature. We define the packing fraction as  $\phi \equiv \pi N r_0^2 / L^2$ . We fixed  $J_0 = 1$  and  $U_0 = 4$  so that both potentials are equal at half-range. Finally,  $K$  is the coupling constant that controls the strength of the spin-velocity coupling, the term that breaks the Galilean invariance and leads to collective motion.

In the main text, we scale the dynamic variables, space-time variables, and parameters according to the transformations  $\mathbf{r}/\sqrt{I/m} \rightarrow \mathbf{r}$ ,  $t/\sqrt{I/J_0} \rightarrow t$ ,  $K/\sqrt{mJ_0} \rightarrow K$ ,  $L/J_0 \rightarrow L$ ,  $U_0/J_0 \rightarrow U_0$ , and we absorb  $U_0$  in the definition of the two-body potential  $U$ . In the Hamiltonian formalism the Lagrangian (1) transforms into

$$\mathcal{H} = \sum_{i=1}^N \frac{1}{2} \mathbf{p}_i^2 + \sum_{i=1}^N \frac{1}{2} \omega_i^2 - \sum_{i=1}^N K \mathbf{p}_i \cdot \mathbf{s}_i + \frac{1}{2} \sum_{k \neq i} U(r_{ik}) - \frac{1}{2} \sum_{k \neq i} J(r_{ik}) \cos \theta_{ik}, \quad (3)$$

where we defined the canonical momenta  $\omega_i = \dot{\theta}_i$  and  $\mathbf{p}_i = \dot{\mathbf{r}} + K \mathbf{s}_i$ .

## III. NUMERICAL METHODS

We simulate the dynamics starting from random states with uniformly distributed  $\{\mathbf{r}_i, \theta_i\}_{i=1..N}$  and  $\{\mathbf{p}_i, \omega_i\}_{i=1..N}$  drawn from centered, reduced Gaussian distributions. Such initial states were placed into a square box with periodic boundary conditions and, after giving some time for the dynamics to settle in, are subjected to a numerical annealing to prepare colder equilibrated states. Numerical annealings are performed by multiplying all rotational velocities by  $\lambda_A = 0.9999$  every 100 time units in our adimensionalized variable, with an integration time step equal to  $\delta t = 10^{-3}$  in the same units. This method enables us to reach low-energy states which, if the cooling is slow enough, should be equilibrium states of the system. Mean values are computed over  $10^2 - 10^3$  independent configurations.

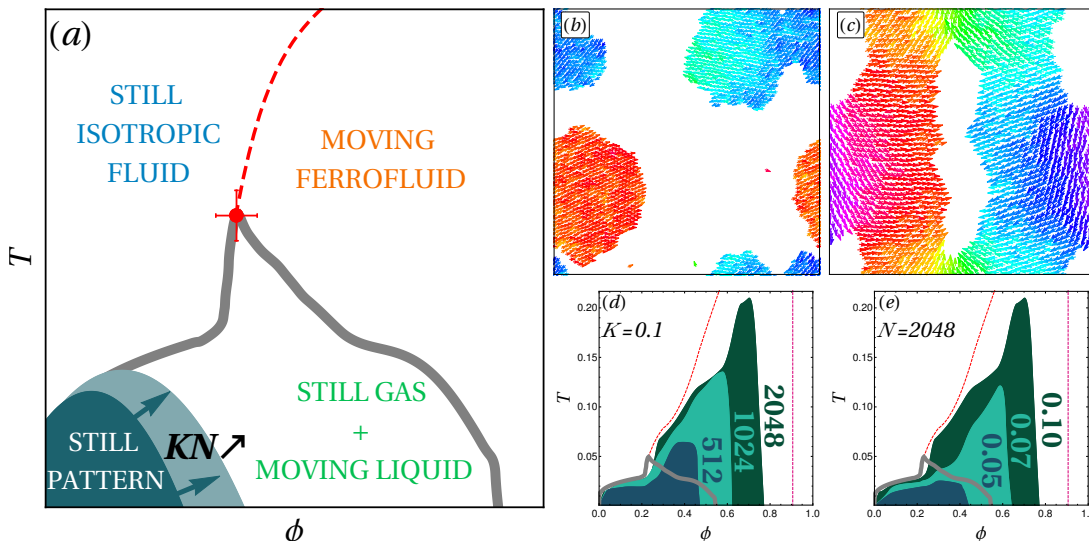


FIG. 1. **Density-Temperature phase diagram.** (a) Sketch of the finite-size phase diagram in the packing fraction, temperature plane, for a low value of  $KN$ . Increasing the value of  $KN$  bloats the patterned region with a small  $m$ . (b) – (c) Examples of spin maps of low-temperature ( $T \approx 0.01$ ) patterned phase-separated states: 2 anti-magnetized droplets obtained for  $N = 2048, K = 0.05, \phi = 0.20$ , and opened up vortices obtained for  $N = 2048, K = 0.05, \phi = 0.40$ . Spins are colored depending on their orientation. (d) – (e) Extent of the patterned regions, as obtained from simulations when varying (d)  $N$  at a fixed  $K = 0.1$ , or (e)  $K$  at a fixed  $N = 2048$ . The boundaries of the patterned states are obtained by visual inspection of states obtained by slow annealings, for 16 different values of the packing fraction in the interval  $0 < \phi \leq 0.8$ .

#### IV. DENSITY-TEMPERATURE PHASE DIAGRAM

We showed in Ref. [3] that, in the case  $K = 0$ , the model described by the Hamiltonian (3) features a phase separation between a ferromagnetic liquid and a paramagnetic gas at low densities and temperatures. This phase separation, which is observed even when the pairwise potential  $U(r)$  is purely repulsive, is induced by the ferromagnetic coupling  $J(r)$ . Indeed, a  $J(r)$  that decreases as  $r$  increases creates an effective attraction between aligned spins, that is sufficient to cause phase separation, that we coined Ferromagnetism-Induced Phase Separation (FIPS)<sup>3</sup>. Because  $J$  is the only source of attraction in the system, we also showed that the left-most spinodal of the liquid-gas phase separation was the lower part of the finite-size Curie line, so that a tricritical point sits at the top of the coexistence line, which presents a cusp.

For  $K > 0$ , a phase separation between a liquid and a gas is still expected at low densities and temperatures, since the spin-mediated attraction between particles is not affected by the presence of a spin-velocity coupling. Furthermore, we showed in Ref. [2] that increasing  $K$  or  $N$  in homogeneous states increases the cost associated to the kinetic energy. As a result, there is a crossover from polar, moving states to states that contain patterns in the magnetization field such that  $m = v_G = 0$  as  $T \rightarrow 0$ , like vortices or solitons, thereby avoiding the kinetic energy cost of a global velocity. This mechanism should also apply to phase-separated domains, as it only relies on energetic arguments, so that we expect phase-separated, still, patterned states. It is *a priori* hard to predict all the possible patterns of such states. However, increasing the density at a constant temperature, and for given values of  $K$  and  $N$ , one intuitively expects the mean number of neighbours of each particle to increase. As a result, curving the magnetization field should become more and more costly as the density increases. Therefore, one expects a domain of still, “patterned” states at low densities and temperatures, that grows as  $K$  or  $N$  is increased. This picture is schematically drawn atop the coexistence line and Curie line from Ref. [3] in Fig. 1(a).

In order to check this picture, we simulate systems at various packing fractions, and for a few sets of values of  $K$  and  $N$ . At low densities, we do observe a rather large zoology of patterned phase-separated states, two examples of which are shown in Fig. 1(b) – (c). At very low densities (close to the left-most side of the coexistence line), as illustrated by Fig. 1(b), the system can organize into two anti-magnetized droplets, and thus replace the energetic cost linked to curving the magnetization field by a surface tension cost. At higher densities, closer to the right-most side of the coexistence line, patterns reminiscent of those observed in the homogeneous case are observed, as illustrated by Fig. 1(c). This configuration resembles the vortex configurations described in the homogeneous case in Ref. [2], but where the system decreased the cost of the magnetic pattern by “unzipping” the line between two of the vortices, thereby creating a hole with no topological charge. The holes at the cores of the two remaining topological defects are



also enlarged, as ill-aligned spins are more repulsive. We also report in Fig. 1(d), (e) the location of such patterned states when varying  $N$  at a fixed  $K$  (Fig. 1(d)), and vice-versa (Fig. 1(e)). These results confirm the picture that increasing  $K$  or  $N$  causes the patterned region to invade the ferromagnetic domains of the phase diagram, starting from the bottom-left corner.

Finally, for all considered values of  $K$  and  $N$ , the patterned domains are clearly below the Curie line at high densities, meaning that the order-by-disorder scenario proposed in Ref. [2] is observed for various values of the density. In fact, it can even be observed in the phase-separated region for sufficiently low values of  $K$  and  $N$ .

## V. DISPLACEMENT-DISPLACEMENT CORRELATIONS IN AN HOMOGENEOUS DISK

In the main text, we present exact curves for the correlation function  $C_d$ . The corresponding calculation was performed in the case of a disk with a homogeneous density  $\rho_0$  and radius  $R$ , rotating around its center at a constant angular velocity  $\Omega$ . In this case, the velocity field can be written in polar coordinates (with the origin at the center of the disk) as

$$\mathbf{v}(\mathbf{r}) = r\Omega \hat{\mathbf{e}}_\theta, \quad (4)$$

where  $\hat{\mathbf{e}}_\theta$  is the unit orthonormal vector at position  $\mathbf{r}$ . By construction, this velocity field has a zero sum over the whole disk. We seek to compute

$$C_d(r) = \frac{1}{c_0} \frac{\sum_{i \neq j} \mathbf{v}_i \cdot \mathbf{v}_j \delta(r_{ij} - r)}{\sum_{i \neq j} \delta(r_{ij} - r)}, \quad (5)$$

where the sum is computed over the particles that constitute the disk, and  $c_0$  ensures that  $C_d(0) = 1$ . These sums can be approximated by integrals that run over the surface of the disk,

$$C_d(r) = \frac{1}{c_0} \frac{\int d^2\mathbf{r}_1 d^2\mathbf{r}_2 \rho(\mathbf{r}_1) \rho(\mathbf{r}_2) \mathbf{v}(\mathbf{r}_1) \cdot \mathbf{v}(\mathbf{r}_2) \delta(r_{12} - r)}{\int d^2\mathbf{r}_1 d^2\mathbf{r}_2 \rho(\mathbf{r}_1) \rho(\mathbf{r}_2) \delta(r_{12} - r)}. \quad (6)$$

Since we here assume the density to be homogeneous, a factor of  $\rho_0^2$  comes out of both integrals, and the density disappears from the calculation altogether. The task at hand is then to compute the integrals in the numerator  $\mathcal{N}$  and the denominator  $\mathcal{D}$  of  $C_d$ , defined by

$$\mathcal{N}(r) \equiv \int d^2\mathbf{r}_1 d^2\mathbf{r}_2 \mathbf{v}(\mathbf{r}_1) \cdot \mathbf{v}(\mathbf{r}_2) \delta(r_{12} - r), \quad (7)$$

$$\mathcal{D}(r) \equiv \int d^2\mathbf{r}_1 d^2\mathbf{r}_2 \delta(r_{12} - r). \quad (8)$$

We first focus on the denominator,  $\mathcal{D}$ . The geometric constraint encoded by the Dirac- $\delta$  can be rewritten explicitly in terms of the polar coordinates of the positions  $\mathbf{r}_1$  and  $\mathbf{r}_2$ , leading to

$$\mathcal{D}(r) = \int_0^R dr_1 \int_0^R dr_2 \int_{-\pi}^{\pi} d\theta_1 \int_{-\pi}^{\pi} d\theta_2 r_1 r_2 \delta\left(r - \sqrt{r_1^2 - r_2^2 + 2r_1 r_2 \cos \theta_{12}}\right), \quad (9)$$

where  $\theta_{12} = \theta_2 - \theta_1$ . One can then use the change of variables  $\theta_2 \rightarrow \theta_2 - \theta_1$ , integrate over  $\theta_1$ , and use the periodicity and parity of the cosine to write

$$\mathcal{D}(r) = 4\pi \int_0^R dr_1 \int_0^R dr_2 \int_0^\pi d\theta r_1 r_2 \delta\left(r - \sqrt{r_1^2 - r_2^2 + 2r_1 r_2 \cos \theta}\right). \quad (10)$$

The integral over the remaining angle can then be computed, using the fact that for any function  $g$  with a single zero at a point  $x_0$ , one has<sup>4</sup>

$$\int_a^b dx f(x) \delta(g(x)) = \frac{f(x_0)}{|g'(x_0)|} \mathbb{1}(a \leq x_0 \leq b), \quad (11)$$

where  $\mathbb{1}$  is a Boolean function which takes the value 1 if its argument is true, and is 0 otherwise. Since the cosine is a bijection from  $[0; \pi]$  to  $[-1; 1]$ , there is *at most* one value  $\theta_0$  of  $\theta$  that verifies the condition imposed by the  $\delta$  in Eq. (10). This value is given by

$$\theta_0 = \arccos \left[ \frac{r_1^2 + r_2^2 - r^2}{2r_1 r_2} \right], \quad (12)$$

and there is such a value in  $[0; \pi]$  if and only if the argument of the arccos is indeed in  $[-1; 1]$ , implying the conditions

$$r^2 \geq (r_1 - r_2)^2, \quad r^2 \leq (r_1 + r_2)^2. \quad (13)$$

Furthermore, we compute the derivative  $g'(\theta_0)$  of the argument  $g(\theta)$  of the Dirac- $\delta$ ,

$$g'(\theta_0) = \frac{r_1 r_2}{r} \sqrt{1 - \left( \frac{r_1^2 + r_2^2 - r^2}{2r_1 r_2} \right)^2}. \quad (14)$$

All in all, integrating over  $\theta$  in Eq. (10) yields

$$\mathcal{D}(r) = 4\pi r \int_0^R dr_1 \int_0^R dr_2 \frac{\mathbb{1}[(r_1 - r_2)^2 \leq r^2 \leq (r_1 + r_2)^2]}{\sqrt{1 - \left( \frac{r_1^2 + r_2^2 - r^2}{2r_1 r_2} \right)^2}}. \quad (15)$$

An equivalent expression is obtained by multiplying the numerator and denominator of the integrand by  $2r_1 r_2$ ,

$$\mathcal{D}(r) = 8\pi r \int_0^R dr_1 r_1 \int_0^R dr_2 r_2 \frac{\mathbb{1}[(r_1 - r_2)^2 \leq r^2 \leq (r_1 + r_2)^2]}{\sqrt{-r_2^4 + 2r_2^2(r_1^2 + r^2) - (r_1^2 - r^2)^2}}. \quad (16)$$

We then change variables according to  $r_2 \rightarrow u = r_2^2$ , and notice that the square root in the denominator is a degree-two polynomial in  $u$ , with roots  $u_{\pm} = (r \pm r_1)^2$ . Furthermore, the conditions in the numerator can be expressed as constraints on  $u$  rather than on  $r$ , yielding  $u_- \leq u \leq u_+$  (which ensures that the content of the square root is positive), so that

$$\mathcal{D}(r) = 4\pi r \int_0^R dr_1 r_1 \int_0^{R^2} du \frac{\mathbb{1}[u_- \leq u \leq u_+]}{\sqrt{-(u - u_+)(u - u_-)}}. \quad (17)$$

It is now convenient to use the conditions in the Boolean function to split the integral over  $u$  into several domains. First, since  $u_- \geq 0$ , the lower bound of the integral over  $u$  is in fact always  $u_-$ . Furthermore, for the integration domain to have a finite extent, one should have  $u_- \leq R^2$ , which imposes  $r_1 \geq r - R$ . Finally, the upper bound of the integral over  $u$ , is the lower of the two values  $R^2$  and  $u_+$ . Stating that  $u_+ \leq R^2$  is equivalent to stating that  $r_1 \leq R - r$ . Therefore, the  $2d$  integration domain naturally splits into two parts: one such that  $r_1 \leq R - r$  (provided that  $r \leq R$ ) so that  $u$  reaches  $u_+$ ; and one such that  $r_1 \geq R - r$  (regardless of the value of  $r$ ) so that  $u$  reaches  $R^2$  before  $u_+$ . In the end, one gets

$$\mathcal{D}(r) = 4\pi r \left[ \mathbb{1}(r \leq R) \int_0^{R-r} dr_1 r_1 \int_{u_-}^{u_+} du \frac{1}{\sqrt{-(u - u_+)(u - u_-)}} + \int_{|R-r|}^R dr_1 r_1 \int_{u_-}^{R^2} du \frac{1}{\sqrt{-(u - u_+)(u - u_-)}} \right]. \quad (18)$$

To compute the integrals over  $u$ , we introduce the change of variables  $u = u_- \cos^2 \phi + u_+ \sin^2 \phi$ . The corresponding differential elements are related by the equation

$$du = 2 \cos \phi \sin \phi (u_+ - u_-) d\phi, \quad (19)$$

and the polynomial in the square root can be rewritten as

$$-(u - u_+)(u - u_-) = (u_+ - u_-)^2 \cos^2 \phi \sin^2 \phi. \quad (20)$$

Finally, the bounds of the integral are given by

$$\phi_R = \arcsin \left[ \sqrt{\frac{R^2 - u_-}{u_+ - u_-}} \right], \quad (21)$$

$$\phi_- = 0, \quad (22)$$

$$\phi_+ = \frac{\pi}{2}, \quad (23)$$

when  $u = R^2$ ,  $u = u_-$ , and  $u = u_+$ , respectively. With all these transformations, Eq. (18) can be rewritten as

$$\mathcal{D}(r) = 8\pi r \left[ \mathbb{1}(r \leq R) \int_0^{R-r} dr_1 r_1 \int_0^{\pi/2} d\phi + \int_{|R-r|}^R dr_1 r_1 \int_0^{\phi_R} d\phi \right]. \quad (24)$$

The first term is an elementary integration, while the second one, that we shall call  $\mathcal{I}$ , is a bit more challenging. It reads

$$\mathcal{I} \equiv \int_{r_1=|R-r|}^R dr_1 r_1 \arcsin \left[ \sqrt{\frac{R^2 - (r - r_1)^2}{4rr_1}} \right]. \quad (25)$$

An integration by parts, as well as some simplifications yield

$$\mathcal{I} = \left[ \frac{r_1^2}{2} \arcsin \left[ \sqrt{\frac{R^2 - (r - r_1)^2}{4rr_1}} \right] \right]_{|R-r|}^R - \frac{1}{2} \int_{r_1=|R-r|}^R dr_1 r_1 \frac{r^2 - R^2 - r_1^2}{\sqrt{-r_1^4 + 2r_1^2(R^2 + r^2) - (R^2 - r^2)^2}}. \quad (26)$$

The last remaining integral can, like before, be treated by first introducing the variable  $v = r_1^2$  and then writing  $v = v_- \cos^2 \phi + v_+ \sin^2 \phi$ , with  $v_{\pm} \equiv (r \pm R)^2$ . Applying these changes one can finally calculate the remaining integral and obtain an explicit expression for the denominator  $\mathcal{D}$ ,

$$\mathcal{D}(r) = \pi r R^2 \left( \pi - \frac{r}{R} \sqrt{4 - \frac{r^2}{R^2}} + 4 \operatorname{arccsc} \frac{2}{\sqrt{2 - r/R}} - 2 \arctan \frac{r/R}{\sqrt{4 - r^2/R^2}} \right). \quad (27)$$

Note that this function is closely related to the pair correlation function in the disk. The latter is essentially recovered by dividing  $\mathcal{D}$  by a factor of  $2\pi r$ .

We now turn our attention to the numerator  $\mathcal{N}(r)$ . Following the same steps that led to Eq. (10) one deduces

$$\mathcal{N}(r) = 4\pi\omega^2 \int_0^R dr_1 \int_0^R dr_2 \int_0^{\pi} d\theta r_1^2 r_2^2 \cos \theta \delta \left( r - \sqrt{r_1^2 - r_2^2 + 2r_1 r_2 \cos \theta} \right). \quad (28)$$

The integration over  $\theta$  can be treated in the same way as for  $\mathcal{D}$ , leading to the expression

$$\mathcal{N}(r) = 2\pi r \omega^2 \int_0^R dr_1 \int_0^R dr_2 \frac{r_1^2 + r_2^2 - r^2}{\sqrt{1 - \left( \frac{r_1^2 + r_2^2 - r^2}{2r_1 r_2} \right)^2}} \mathbb{1} \left[ (r_1 - r_2)^2 \leq r^2 \leq (r_1 + r_2)^2 \right]. \quad (29)$$

The changes of variables  $u = r_2^2$  and  $u = u_- \cos^2 \phi + u_+ \sin^2 \phi$ , with the same definitions as before, then leads to

$$\begin{aligned} \mathcal{N}(r) &= 4\pi r \omega^2 \int_0^{R-r} dr_1 r_1 \int_0^{\pi/2} d\phi \left[ (r_1^2 - r^2) + u_- \cos^2 \phi + u_+ \sin^2 \phi \right] \mathbb{1} [r \leq R] \\ &\quad + 4\pi r \omega^2 \int_{|R-r|}^R dr_1 r_1 \int_0^{\phi_R} d\phi \left[ (r_1^2 - r^2) + u_- \cos^2 \phi + u_+ \sin^2 \phi \right]. \end{aligned} \quad (30)$$

The first integral is, again, simple to compute. The second one, that we shall call  $\mathcal{J}$ , can be rewritten using the expression of  $\phi_R$  and some trigonometry ( $\sin 2\theta_R = 2 \cos \theta_R \sin \theta_R$  and  $\cos \arcsin x = \sqrt{1-x^2}$ ),

$$\begin{aligned} \mathcal{J} &\equiv \int_{|R-r|}^R dr_1 r_1 \int_0^{\phi_R} d\phi [(r_1^2 - r^2) + u_- \cos^2 \phi + u_+ \sin^2 \phi] \\ &= 2 \int_{|R-r|}^R dr_1 r_1^3 \arcsin \sqrt{\frac{R^2 - (r-r_1)^2}{4rr_1}} - 2r \int_{|R-r|}^R dr_1 r_1^2 \sqrt{1 - \frac{R^2 - (r-r_1)^2}{4rr_1}} \sqrt{\frac{R^2 - (r-r_1)^2}{4rr_1}}. \end{aligned} \quad (31)$$

The first term in  $\mathcal{J}$  is similar to  $\mathcal{I}$ : the only difference is that there is an extra factor of  $r_1^2$ . The second term, on the other hand, can be rewritten using the variable  $v = r_1^2$ , as

$$\int_{|R-r|}^R dr_1 r_1^2 \sqrt{1 - \frac{R^2 - (r-r_1)^2}{4rr_1}} \sqrt{\frac{R^2 - (r-r_1)^2}{4rr_1}} = \frac{1}{8r} \int_{(R-r)^2}^{R^2} dv \sqrt{-(v-v_+)(v-v_-)} \quad (32)$$

and can be integrated using techniques similar to those presented above. The numerator  $\mathcal{N}$  can then be written as

$$\begin{aligned} \mathcal{N}(r) &= \frac{\pi\omega^2 R^4}{4} r \left[ \pi \left( 2 - 4 \frac{r^2}{R^2} \right) + \frac{r}{R} \sqrt{4 - \frac{r^2}{R^2}} \left( \frac{r^2}{R^2} - 6 \right) + 16 \frac{r^2}{R^2} \operatorname{arccot} \sqrt{\frac{2-r/R}{2+r/R}} \right. \\ &\quad \left. + 8 \operatorname{arccsc} \frac{2}{\sqrt{2-r/R}} - 4 \left( 1 + 2 \frac{r^2}{R^2} \right) \arctan \frac{r/R}{\sqrt{4-r^2/R^2}} \right]. \end{aligned} \quad (33)$$

One can check that  $\int_0^{2R} dr \mathcal{N}(r) = 0$ , which follows from  $\sum_i \mathbf{v}_i = \mathbf{0}$ .<sup>5</sup>

Putting  $\mathcal{N}$  and  $\mathcal{D}$  back together, we derive an expression for  $C_d$ . In order to have  $C_d(0) = 1$ , one should set  $c_0 = R^2\omega^2/4$ . When replacing  $c_0$  by this value, the expression for  $C_d$  turns out to only depend on  $x = r/(2R)$ , and it reads

$$C_d(x) = \frac{\pi(2-16x^2) + 4x\sqrt{1-x^2}(2x^2-3) + 64x^2 \operatorname{arccot} \sqrt{\frac{1-x}{1+x}} + 8 \operatorname{arccsc} \frac{1}{\sqrt{1-x}} - 4(1+8x^2) \arctan \frac{x}{\sqrt{2-2x^2}}}{\pi - 4x\sqrt{1-x^2} + 4 \operatorname{arccsc} \frac{1}{\sqrt{1-x}} - 2 \arctan \frac{x}{\sqrt{2-2x^2}}}. \quad (34)$$

As mentioned in the main text, this function only depends on distance through its ratio to the size of the system. Since this function is rather cumbersome, one can also Taylor-expand it around 0 up to order 2, finding

$$C_d(x) \approx 1 - \frac{4}{\pi}x - \frac{16}{\pi^2}x^2. \quad (35)$$

This expression is a rather good approximation of  $C_d$  in the  $[0; 1]$  interval. In particular, it has a root at

$$x_0 = \frac{\pi}{8}(\sqrt{5}-1) \approx 0.485. \quad (36)$$

It is tempting to reproduce the calculation above in the case of the speed-speed correlation  $C_{sp}$ . In the case of a homogeneous disk, noticing that

$$\frac{1}{N} \sum_i \mathbf{v}_i \approx \frac{1}{\pi R^2} \int d^2 \mathbf{r} r \boldsymbol{\omega} = \frac{2}{3} R \boldsymbol{\omega}, \quad (37)$$

the full speed-speed correlation can be written as

$$C_{sp}(r) = \frac{\omega^2}{c_{0,sp} \mathcal{D}(r)} \int d^2 \mathbf{r}_1 d^2 \mathbf{r}_2 \left( r_1 - \frac{2}{3} R \right) \left( r_2 - \frac{2}{3} R \right) \delta(r - r_{12}) \quad (38)$$

$$= \frac{\omega^2}{c_{0,sp} \mathcal{D}(r)} \int d^2 \mathbf{r}_1 d^2 \mathbf{r}_2 \left( r_1 r_2 - \frac{4}{3} R r_1 + \frac{4}{9} R^2 \right) \delta(r - r_{12}). \quad (39)$$

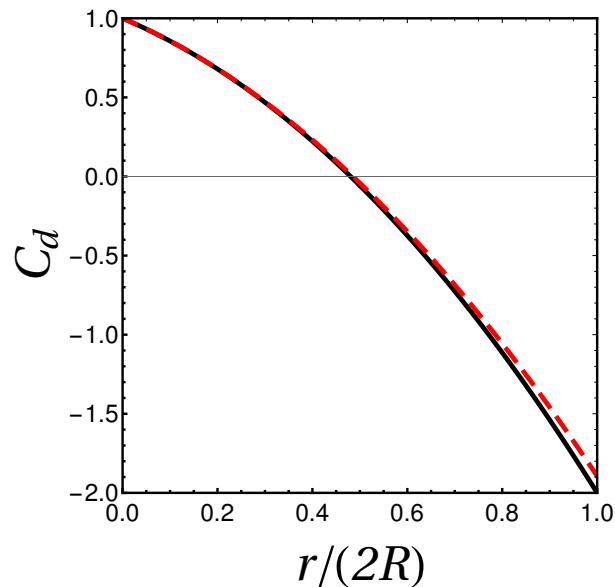


FIG. 2. **Exact displacement-displacement correlations in a rotating homogenous disk.** We show here a plot of the exact expression (34) (black line), and its Taylor expansion to second order around 0 (dashed red line), as given by Eq. (35).

While the last two terms in the integral in the numerator can be computed using the strategies used for  $C_d$ , the first term is in fact much less tractable. Indeed, if we call

$$\mathcal{N}_{sp}^1(r) \equiv \omega^2 \int d^2\mathbf{r}_1 d^2\mathbf{r}_2 r_1 r_2 \delta(\mathbf{r} - \mathbf{r}_{12}), \quad (40)$$

following the same route as for  $\mathcal{N}$  yields

$$\mathcal{N}_{sp}^1(r) = 8\pi r \omega^2 \int_0^R dr_1 r_1^2 \int_0^{R^2} du \frac{\sqrt{u}}{\sqrt{-(u-u_+)(u-u_-)}} \mathbb{1}[u_- \leq u \leq u_+]. \quad (41)$$

Here, the most convenient change of variable is the one used for the other integrals, but where  $u_+$  and  $u_-$  are swapped,

$$u = u_+ \cos^2 \phi + u_- \sin^2 \phi. \quad (42)$$

Indeed, using this definition, after some more algebra, one finds

$$\begin{aligned} \mathcal{N}_{sp}^1(r) = & 8\pi r \omega^2 \int_0^{R-r} dr_1 r_1^2 (r+r_1) E\left(\frac{4rr_1}{(r+r_1)^2}\right) \mathbb{1}[r \leq R] \\ & + 8\pi r \omega^2 \int_{|r-R|}^R dr_1 r_1^2 (r+r_1) \left[ E\left(\frac{4rr_1}{(r+r_1)^2}\right) - E\left(\varphi_R, \frac{4rr_1}{(r+r_1)^2}\right) \right], \end{aligned} \quad (43)$$

where  $E(\varphi, x)$  is the incomplete elliptic integral of the second kind,<sup>6</sup>  $E(x) = E(\pi/2, x)$  is the elliptic integral of the second kind, and

$$\varphi_R \equiv \arcsin \sqrt{\frac{u_+ - R^2}{u_+ - u_-}}. \quad (44)$$

Since elliptic functions are in general hard and cumbersome to treat analytically, there is little hope of writing a tractable expression for  $C_{sp}$  using this integration strategy. However, one still expects an expression that only depends on  $r/(2R)$ : changing variables following  $r_{1,2} \rightarrow 2R x_{1,2}$  in every integral of  $C_{sp}$  yields a  $R^2 \omega^2$  prefactor that should be absorbed by  $c_{0,sp}$ , like in the case of  $C_d$ .

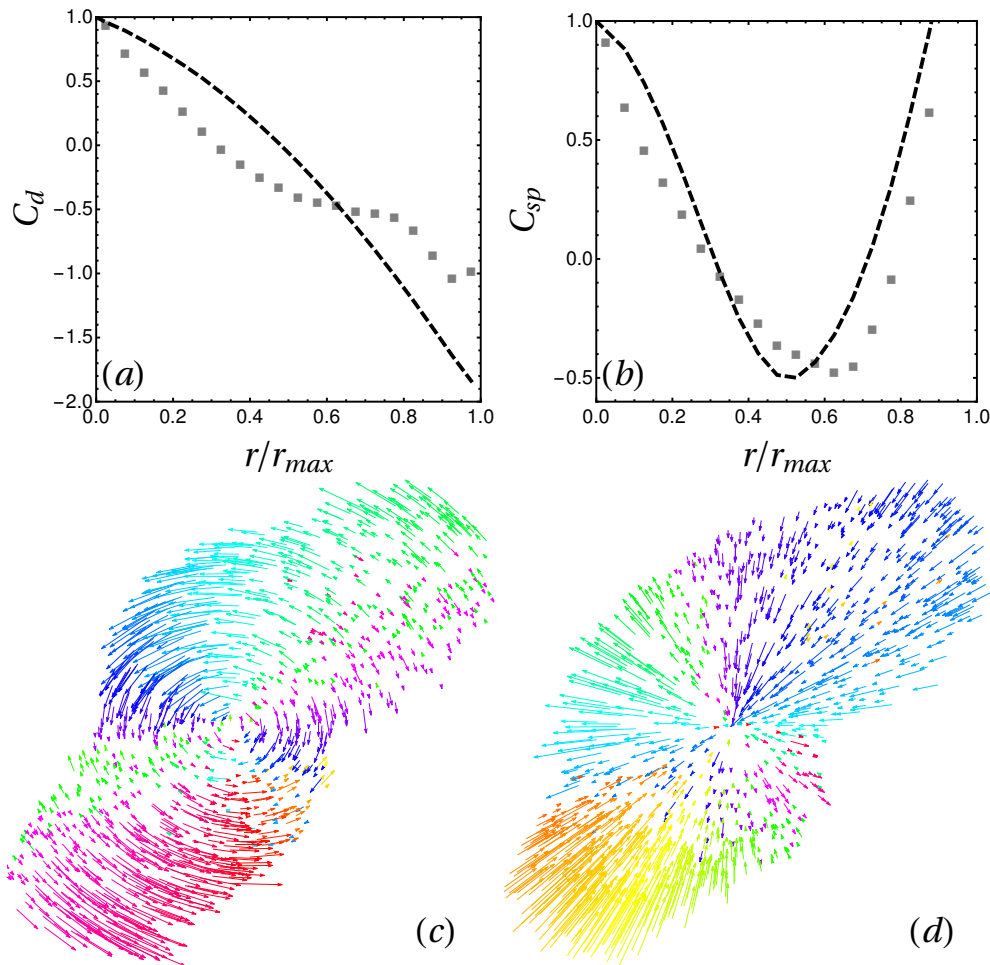


FIG. 3. **Bird Displacement Fluctuations.** (a) Displacement correlations  $C_d(r, \tau)$  against distance normalized by the largest distance in the flock, computed from the SI of Ref. [5]. (b) Corresponding curves for  $C_{sp}$ . The dashed black lines are numerical estimations for a homogeneous disk rotating at a constant speed. (c) Azimuthal displacement fluctuations around the main rotation axis in the flock, color-coded according to their direction. (d) Projected radial displacement fluctuations around the centre of mass of the flock, as seen from above the main rotation axis.

## VI. CORRELATIONS IN FLOCKS OF BIRDS

In order to compare our results to real flocks, we use the data in the SI of Ref. [5]. From this data, we compute  $C_d$  and  $C_{sp}$  yielding the curves in Fig. 3(a) – (b). Their shape is different from the shapes shown in the main text. This difference can be attributed to either of three reasons:

(i) Firstly, the density in flocks is not homogeneous: it is higher near the boundary<sup>7</sup>. Intuitively, this density profile, compared to the homogeneous case, should lead to lower absolute values of the correlation functions at long distances, and shift the curves off-center. These intuitive consequences are compatible with the shift between the observations and the calculation in the case of a homogeneous disk shown in Fig. 3(a) – (b).

(ii) Secondly, flocks are not perfectly circular, they are generally elliptic in the two directions of large extension, which should mostly move the zero of the correlation functions off-center.

(iii) Thirdly, and most importantly, the displacement fields can have other components than simple rotations. To measure the importance of this last effect, we use the same data and seek the main rotation axis ( $\Delta$ ), by computing the sum  $\sum \mathbf{r}_i \times \mathbf{v}_i$ . We then use this axis as the zenith direction of a spherical coordinate system, centered on the centre of mass of the flock, and we decompose the displacement fluctuations into their radial, polar, and azimuthal components. We find that the polar component (carried by the  $\hat{\mathbf{e}}_\theta$  unit vector in polar coordinates) is typically much smaller than the other two, so that we omit it in this discussion. The azimuthal component (carried by the  $\hat{\mathbf{e}}_\phi$  unit vector in polar coordinates) contains the rotation part of the displacements around the chosen zenith direction. The measured field, with all birds represented in the plane perpendicular to  $\Delta$  is plotted in Fig. 3(c), with a rescaling

factor such that all displacements are visible. Although it is not a perfect solid rotation, this picture shows that there is indeed some rigid rotation in the flock, which could account for correlations akin to those observed in our system. Finally, the radial component, which contains the dilatation and compression parts of the displacement field, is plotted in Fig. 3(d), at the same scale as the azimuthal field. This picture shows that the radial component is locally as large as the azimuthal one, so that it could modify the shape of the displacement-displacement correlations. Additionally, it roughly assumes the shape of a quadrupolar field: the long direction of the flock is compressed, and the short one expanded. If this shape is a general one across different flocks, it would mean that flocks of birds have a finite Poisson ratio, a property of elastic solids<sup>8</sup>. This finite elasticity could also partly explain the difference between the correlation curves observed in natural flocks and the ones obtained in the Hamiltonian flocks studied in this Letter. Indeed, while Hamiltonian flocks are defined with finite-range, metric interactions, birds interact with non-metric (typically visual) interactions<sup>9</sup>, that intuitively allow for stronger elastic effects, since the distances between birds are not fixed by an underlying potential.

---

\* [casiulis@lptmc.jussieu.fr](mailto:casiulis@lptmc.jussieu.fr)

<sup>1</sup> S. L. Bore, M. Schindler, K.-D. N. T. Lam, E. Bertin, and O. Dauchot, *J. Stat. Mech. Theory Exp.* **2016**, 033305 (2016).

<sup>2</sup> M. Casiulis, M. Tarzia, L. F. Cugliandolo, and O. Dauchot, *Arxiv Prepr.*, 1905.0857 (2019).

<sup>3</sup> M. Casiulis, M. Tarzia, L. F. Cugliandolo, and O. Dauchot, *J. Chem. Phys.* **150**, 154501 (2019).

<sup>4</sup> I. Gel'Fand and G. Shilov, *Generalized Functions, Vol. 1* (Academic Press, 1968).

<sup>5</sup> A. Cavagna, A. Cimorelli, I. Giardina, G. Parisi, R. Santagati, F. Stefanini, and M. Viale, *Proc. Natl. Acad. Sci.* **107**, 11865 (2010).

<sup>6</sup> M. Abramowitz and I. A. Stegun, *Handbook of Mathematical Functions* (National Bureau of Standards, Applied Mathematics Series, 1972).

<sup>7</sup> M. Ballerini, N. Cabibbo, R. Candelier, A. Cavagna, E. Cisbani, I. Giardina, A. Orlandi, G. Parisi, A. Procaccini, M. Viale, and V. Zdravkovic, *Anim. Behav.* **76**, 201 (2008).

<sup>8</sup> L. D. Landau and E. M. Lifshitz, *Course of Theoretical Physics Vol. 7: Theory of Elasticity*, 3rd ed. (Pergamon Press, 1986).

<sup>9</sup> W. Bialek, A. Cavagna, I. Giardina, T. Mora, E. Silvestri, M. Viale, and A. M. Walczak, *Proc. Natl. Acad. Sci.* **109**, 4786 (2012).